Redox Biology 67 (2023) 102877

Contents lists available at ScienceDirect

Redox Biology

journal homepage: www.elsevier.com/locate/redox

FGF21 alleviates adipose stem cell senescence via CD90 glycosylation-dependent glucose influx in remodeling healthy white adipose tissue

Zixin Zhou [a,1], Huiying Zhang [a,1], Yan Tao [a], Jinhao Zang [a], Jingyuan Zhao [a], Huijie Li [a], Yalin Wang [a], Tianci Wang [a], Hui Zhao [b], Fuwu Wang [c], Chun Guo [a], Faliang Zhu [a], Haiting Mao [b], Fengming Liu [a], Lining Zhang [a], Qun Wang [a,*]

[a] Key Laboratory of Infection and Immunity of Shandong Province, Department of Immunology, School of Basic Medical Sciences, Cheeloo College of Medicine, Shandong University, Jinan, 250012, China
[b] Department of Clinical Laboratory, The Second Hospital, Cheeloo College of Medicine, Shandong University, Jinan, 250033, China
[c] Key Laboratory for Experimental Teratology of Ministry of Education, Shandong Key Laboratory of Mental Disorders, Department of Histology and Embryology, School of Basic Medical Sciences, Cheeloo College of Medicine, Shandong University, Jinan, 250012, China

ARTICLE INFO

Keywords:
Adipose stem cell senescence
Reactive oxygen species
Glucose metabolism
FGF21
CD90
Adipose tissue

ABSTRACT

The senescence of adipose stem cells (ASCs) impairs healthy adipose tissue remodeling, causing metabolic maladaptation to energy surplus. The intrinsic molecular pathways and potential therapy targets for ASC senescence are largely unclear. Here, we showed that visceral ASCs were prone to senescence that was caused by reactive oxygen species (ROS) overload, especially mitochondrial ROS. These senescent ASCs failed to sustain efficient glucose influx, pentose phosphate pathway (PPP) and redox homeostasis. We showed that CD90 silence restricted the glucose uptake by ASCs and thus disrupted their PPP and anti-oxidant system, resulting in ASC senescence. Notably, fibroblast growth factor 21 (FGF21) treatment significantly reduced the senescent phenotypes of ASCs by augmenting CD90 protein via glycosylation, which promoted glucose influx via the AKT-GLUT4 axis and therefore mitigated ROS overload. For diet-induced obese mice, chronic administration of low-dose FGF21 relieved their visceral white adipose tissue (VAT) dysfunction and systemic metabolic disorders. In particular, VAT homeostasis was restored in FGF21-treated obese mice, where ASC repertoire was markedly recovered, accompanied by CD90 elevation and anti-senescent phenotypes in these ASCs. Collectively, we reveal a molecular mechanism of ASC senescence by which CD90 downregulation interferes glucose influx into PPP and redox homeostasis. And we propose a FGF21-based strategy for healthy VAT remodeling, which targets CD90 glycosylation to correct ASC senescence and therefore combat obesity-related metabolic dysfunction.

1. Introduction

White adipose tissue (WAT) is a highly plastic organ that regulates energy metabolism in response to different nutritional states. Adipose mesenchymal stem cells (ASCs) are critical adipocyte progenitors that possess adipogenic potential and immunoregulatory function to facilitate WAT homeostasis [1–5]. Upon energy surplus, ASCs sustain effective adipocyte hyperplasia to drive healthy WAT remodeling. For morbid obesity, the decline of ASC function is accompanied by pathological WAT remodeling, including aberrant adipocyte hypertrophy, inflammation and fibrosis, which eventually cause WAT dysfunction and systemic metabolic disorders [1,2,6].

Visceral WAT (VAT) is more vulnerable to pathological remodeling compared with subcutaneous WAT (SAT). And consistently, *in vitro* cultured visceral ASCs (V-ASCs) had lower proliferative and adipogenic potentials than subcutaneous ASCs (S-ASCs), despite that *in vivo* adipogenesis differs with fat depots, nutritional or metabolic states [7–10]. It remains elusive if some intrinsic features endow ASCs with distinct

* Corresponding author. Department of Immunology, School of Basic Medical Sciences, Cheeloo College of Medicine, Shandong University, 44 Wenhua Xi Road, Jinan, 250012, China.
E-mail address: wangqun@sdu.edu.cn (Q. Wang).
[1] These authors contribute equally to this work.

https://doi.org/10.1016/j.redox.2023.102877
Received 9 August 2023; Received in revised form 4 September 2023; Accepted 4 September 2023

metabolic decisions and thus different potentials. Recently, the accumulation of senescent cells, including ASCs, was found in VAT of obese mice; depletion of these cells could alleviate WAT dysfunction and metabolic disorders [11,12]. Similarly, ASCs from obese or aged individuals with insulin resistance showed impairment in adipogenic capacity accompanied by senescent phenotypes, thus linking ASC senescence with metabolic risks [13,14]. Cellular senescence is a status of cell cycle arrest, as manifested by proliferation restriction [15,16]. Our previous study showed that CD90, a stem cell-related marker on ASCs, affected the proliferation and adipogenic differentiation of ASCs [17], whereas its relationship with ASC senescence is still unclear. More recently, we found a subset of CX3CR1^{high} macrophages that could restrict the senescent phenotypes of ASCs, including cycle inhibitors P53, P21, P16 and senescence-associated β galactosidase (SAβgal) activity, thereby maintaining VAT homeostasis [18]. However, aside from these external factors, intrinsic determinators and distinct metabolic pathways during ASC senescence deserve further investigation. The potential therapy targets and strategies that combat ASC senescence remain to be explored.

Fibroblast growth factor 21 (FGF21) is a newly discovered FGF family member that is induced by nutritional or stress signals like extended starvation, high sugar intake or dietary protein restriction. In physiological condition, circulation FGF21 is primarily derived from liver that regulates energy metabolism through acting on multiple metabolic tissues or organs [19,20]. FGF21 treatment was used to reduce body weight or correct metabolic disorders in animal models with obesity, diabetes or non-alcoholic steatohepatitis. But there were still some obstacles in its clinical application, such as undesired *in vivo* effects probably caused by high-dosage treatment or uncertain action targets [21,22]. FGF receptor 1 (FGFR1) and its co-receptor β-Klotho have been detected in multiple tissues including fat, liver, pancreas and hypothalamus, whereas precise cellular targets of FGF21 in these tissues have not yet been fully revealed. As in its regulation on WAT metabolism, adipocytes, more specifically, 3T3L1-differentiated adipocytes are the only validated cell population targeted by FGF21 [23,24]. It remains largely unclear whether and how FGF21 regulates ASCs in WAT remodeling.

In this study, we provided evidence that V-ASCs were prone to senescence caused by redox imbalance. Mechanistically, CD90 acted as a valve for glucose influx into ASCs, whose downregulation disrupted glucose metabolism-dependent redox homeostasis and thus induced ASC senescence. Importantly, FGF21 was identified to target CD90 glycosylation expression, which boosted glucose influx to eliminate reactive oxygen species (ROS) and relieve ASC senescence. Chronic administration of low-dose FGF21 effectively rescued ASC senescence to drive healthy VAT remodeling, thereby mitigating metabolic disorders in obese mice.

2. Materials and methods

2.1. Animals

Male C57BL/6J mice were purchased from Vital River Laboratory Animal Technology (Beijing, China). All mice were maintained on a 12:12-h light-dark cycle and an ambient temperature of 22 °C ± 2 °C. Animal care was approved by Ethics Committee of School of Basic Medical Sciences, Shandong University. All experimental procedures were performed on male mice and complied with the institutional guidelines. For animal models with VAT dysfunction and *in vivo* FGF21 treatment, male mice at 8 weeks of age were fed with normal chow diet (NCD) or high fat diet (HFD; TP23300, 60 kcal% fat, 19.4 kcal% protein, 20.6 kcal% carbohydrate, Trophic, Nantong, China) for 15 weeks; FGF21 (0.5 mg/kg body weight) was intraperitoneally injected every 2 days during last 4 weeks of diet intervention, which was defined by referring to previous studies with minor modification [25–27]. Body weight and blood glucose were monitored during the experiment, glucose tolerance test (GTT) and insulin tolerance test (ITT) were performed within 1 week before ending the experiment.

2.2. Metabolic parameters

Random blood glucose levels were measured in mice at 9 a.m. unless it was specified. GTT was performed at 9 a.m. in mice after an overnight fast. ITT was performed at 2 p.m. in mice after a 6 h fast. The levels of blood glucose were measured at different timepoints before and after intraperitoneal injection with glucose (2 g/kg body weight; G7528, Sigma-Aldrich, St. Louis, MO) or human insulin (0.75U/kg body weight, 9004-10-B, Wanbang Biopharmaceuticals, Xuzhou, China). Glucose levels were measured with a drop of tail vein blood using glucometer (One Touch, New Brunswick, NJ).

2.3. Histology and immunofluorescence

Hematoxylin and eosin (H&E) staining was performed in VAT sections as per the procedures. The adipocyte sizes were evaluated by calculating average adipocyte area using ImageJ software by referring to previous studies [28–31]. At least 400 adipocytes were included in randomly selected areas from 2 sections per mouse, 3 mice per group. This method is used for comparing the relative sizes of adipocytes between groups, but there were still limitations in accurately estimating adipocyte sizes, as compared with the calculation of average cross-sectional area of adipocytes in Bargut et al.'s study [32]. Immunofluorescence staining was conducted in VAT sections after dewaxing, dehydrating and blocking with 1% BSA. The sections were incubated with primary antibodies at 4 °C overnight, followed by TRITC- or FITC-conjugated secondary antibodies at 37 °C for 30 min (antibodies listed in Table S1). Cellular immunofluorescence was performed in cells fixed with 4% paraformaldehyde and permeabilized with 0.1% Triton-X (Sigma-Aldrich). After blockade with 1% BSA, the cells were incubated with primary antibodies at 4 °C overnight, followed by TRITC- or FITC-conjugated secondary antibodies at 37 °C for 30 min. Nuclei eres stained with DAPI (C1006, Beyotime, Shanghai, China). Fluorescence signals were photographed by Opera Phenix Plus High-Content Screening System Opera Phenix (PerkinElmer, Wellesley, MA) or confocal microscopy (Zeiss LSM 780, Oberkochen, Germany).

2.4. ASC culture and treatment

Primary ASCs were isolated from inguinal SAT (S-ASCs) or epididymal VAT (V-ASCs) of male mice at 10–12 weeks of age. Briefly, adipose tissue was digested in Krebs-Ringer Bicarbonate buffer containing 2 mg/mL collagenase (LS004196, Worthington, Lakewood, NJ) at 37 °C for about 50 min. After centrifugation, the floated lipid layer was removed and the stromal vascular fraction (SVF) was resuspended in Dulbecco's modified Eagle medium (DMEM; 06-1055-57-1ACS, Biological Industries, Haemek, Israel) supplemented with 10% fetal bovine serum (FBS; BSA10099-141C, Invitrogen, Carlsbad, CA). After culture for 24 h, non-adherent cells were removed and the adherent cells were incubated in complete DMEM containing 10% FBS and 5 ng/mL basic fibroblast growth factor (100-18B, PeproTech, Cranbury, NJ). The 3-5th passage of ASCs were used. For lipopolysaccharide (LPS) stimulation, ASCs were treated with 500 ng/mL LPS for 24 h. In some experiments, ASCs were treated with 10 mM Toll-like receptor 2 (TLR2) inhibitor CUCPT-22 (4884, Tocris Bioscience, England, Bristol) or 10 mM TLR4 inhibitor TAK-242 (HY-11109, MCE, Monmouth, NJ) for 9 h. For AKT blockade, ASCs were treated with 100 nM MK2206 (S1078, Selleck, Houston, TX) for 16 h. For FGF21 stimulation, ASCs were treated with 500 ng/mL FGF21 (100–42, PeproTech) for 6 h, which was defined based on previous studies with minor modification [20,33]; in some condition, ERK was blocked with 50 μM U0126 (S1102, Selleck) 3 h before FGF21 treatment.

2.5. SAβgal activity staining

SAβgal activity was assayed using SAβgal staining kit (cs0030, Sigma-Aldrich; or C0602, Beyotime) based on the manufacturer's instruction. After fixation in fixing solution for 10 min, ASCs were stained with staining buffer containing X-Gal at 37 °C for 6 h while avoiding CO_2 exposure. Senescent cells in blue were visualized by microscopy. Fresh adipose tissues were fixed for 30 min, followed by soaking in staining buffer at 37 °C overnight away from CO_2. Tissue senescence was evaluated based on the degree of the color blue.

2.6. Cellular ROS measurement

Total intracellular or mitochondrial reactive oxygen species (ROS) were examined in ASCs using DCFH-DA (D6883, Sigma-Aldrich) or MitoSOX (M36008, Thermo Fisher, Waltham, MA), respectively. Briefly, ASCs were cultured for 9 h of attachment, followed by incubation with 10 μM DCFH-DA for 30 min or 5 μM MitoSOX for 10 min at 37 °C. Fluorescent signals were detected by flow cytometry (cytoFLEX, Beckman-Couler, Bria, CA). In some experiments, ASCs were cultured in 96-well plate (1×10^4/well) for ROS fluorescence imaging using Opera Phenix Plus High-Content Screening System (PerkinElmer). For ROS elimination, ASCs were treated with 5 mM N-acetylcysteine (NAC, A7250, Sigma-Aldrich) or 5 μM Mito-TEMPO (SML0737, Sigma-Aldrich) for 12 h before related assays.

2.7. Glucose uptake by ASCs

ASCs were cultured in 12-well plate (5×10^5 cells/well) for 16 h. After three washes with PBS, the cells were incubated with glucose-free medium containing 100 μM 2-NBDG (36702, AAT Bioquest, Sunnyvale, CA) at 37 °C for 15 min. After two washes with cold PBS, the cells were detected for fluorescence signals by flow cytometry. In some assays, ASCs transfected with siCD90 or treated with FGF21 were used for glucose uptake assay. For glucose influx blockade, ASCs in 12-well plate (5×10^5/well) were treated with 10 mM 2-Deoxy-D-glucose (2-DG; HY-13966, MCE, NJ) for 8 h.

2.8. G6PDH activity and NADPH/$NADP^+$ measurement

After 9 h of attachment, ASCs were collected for the following assays according to the manufacturer's instructions. G6PDH (glucose-6-phosphate dehydrogenase) activity was examined in cell lysates using G6PDH Activity Assay Kit (S0189, Beyotime) and normalized to total protein contents. NADPH and $NADP^+$ was extracted and measured using NADPH/$NADP^+$ Assay Kit (S0179, Beyotime), the amounts were normalized to total protein contents and NADPH/$NADP^+$ ratio was calculated.

2.9. GSH and GSSG measurement

Glutathione (GSH) and glutathione disulfide (GSSH) were measured using GSH and GSSG Assay Kit (S0053, Beyotime) according to the manufacturer's instruction. Briefly, the harvested ASCs were treated with protein removal reagent, followed by two times of rapid freezing-thawing in liquid nitrogen and 37 °C water-bath successively. After centrifugation at 10000*g* for 10 min at 4 °C, the supernatants were measured for total glutathione or GSSG (after GSH clearance), the amounts were normalized to protein contents. GSH contents and GSH/GSSG ratio were calculated.

2.10. Gene silence by siRNA transfection

ASCs were transfected with siCD90 or siControl (Sigma-Aldrich) using PEI transfection reagent (PR40001, Proteintech, Rosemont, IL) according to the instruction. After 24 or 48 h transfection, the cells were collected for further examination. The knockdown efficiency of siRNA was verified by quantitative PCR. The sequences of specific primers and siRNAs are listed in Tables S2 and S3.

2.11. Flow cytometry

ASCs or SVF from VAT were incubated with Fc block at 4 °C for 15 min and stained with fluorescence-conjugated antibodies against CD90, TLR2, TLR4, CD45, Sca-1 at 4 °C for 30 min. The cells were acquired using CytoFLEX and the data were analyzed by CytExpert (Beckman Coulter). Antibodies are listed in Table S1.

2.12. Cytokine secretion assay by ELISA

ASCs at 8×10^4/well in 12-well plates were cultured for 48 h, the supernatants were determined for cytokine secretion using ELISA kit (1210602 for IL-6, 12-2720-096 for TNF-α, 1217392 for MCP-1; DAKEWEI, Nanjing, China) according to the manufacturer's instructions. In some experiments, LPS was added 24 h before the assay, either, ASCs were treated with siCD90 or siControl for 48 h before the assay.

2.13. Protein N-glycosylation assay

The proteins were extracted using ice-cold RIPA lysis buffer (P0013B, Beyotime) containing inhibitors of protease and phosphatase (P1260-1, Solarbio, Beijing, China) and gently mixed with glycoprotein denaturing buffer (1 M DTT and 5% SDS). After denaturation at 100 °C for 10 min, the proteins were deglycosylated by N-glycosylase (PNGase) F treatment (1μL/50 μg protein; 20411ES01, Yeasen, Shanghai, China) at 37 °C for 2 h. The reactions were stopped by the addition of sample buffer and further incubation at 100 °C for 10 min. The samples were subjected to SDS-PAGE followed by Western blot for target proteins.

2.14. Western blot

Equal amounts protein lysates were subjected to SDS-PAGE electrophoresis and transferred onto PVDF (polyvinylidene fluoride) membrane. The membranes were incubated with primary antibodies at 4 °C overnight, followed by HRP-conjugated secondary antibodies at room temperature for 1 h. The bands were detected with Immobilon ECL Ultra Western HRP substrate (2213702, Sigma-Aldrich) using chemiluminescent imaging system (Tanon, Shanghai, China). Densitometry of the bands was determined using ImageJ software. Antibodies are listed in Table S1.

2.15. Quantitative PCR

Total RNA was extracted using RNA extraction kit (220011, RNAfast200, Fastagen Biotech, Shanghai, China) or TRNzol Universal reagent (DP424, TIANGEN, Beijing, China), and then reversely transcribed into cDNA using ReverTra Ace qPCR RT kit (FSQ-101, Toyobo, Osaka, Japan). UltraSYBR Mixture (CW0957S, CWBIO, Taizhou, China) was used in quantitative PCR in a CFX Connect Real-Time PCR Detection System (Bio-Rad, Hercules, CA). Relative mRNA levels of indicated genes were calculated by $2^{-\Delta\Delta Ct}$ method, using *18s* rRNA or *Gapdh* as internal controls. Primers are listed in Table S2.

2.16. Statistical analysis

Statistical analysis was performed with GraphPad Prism 8.0. Differences between two groups or multiple groups were evaluated by student's *t*-test, one-way or two-way ANOVA, respectively. Data are presented as mean ± SD. $p < 0.05$ was considered statistically significant. The numbers of replicates in each assay or animal samples in each experiment are indicated in corresponding Figure legends.

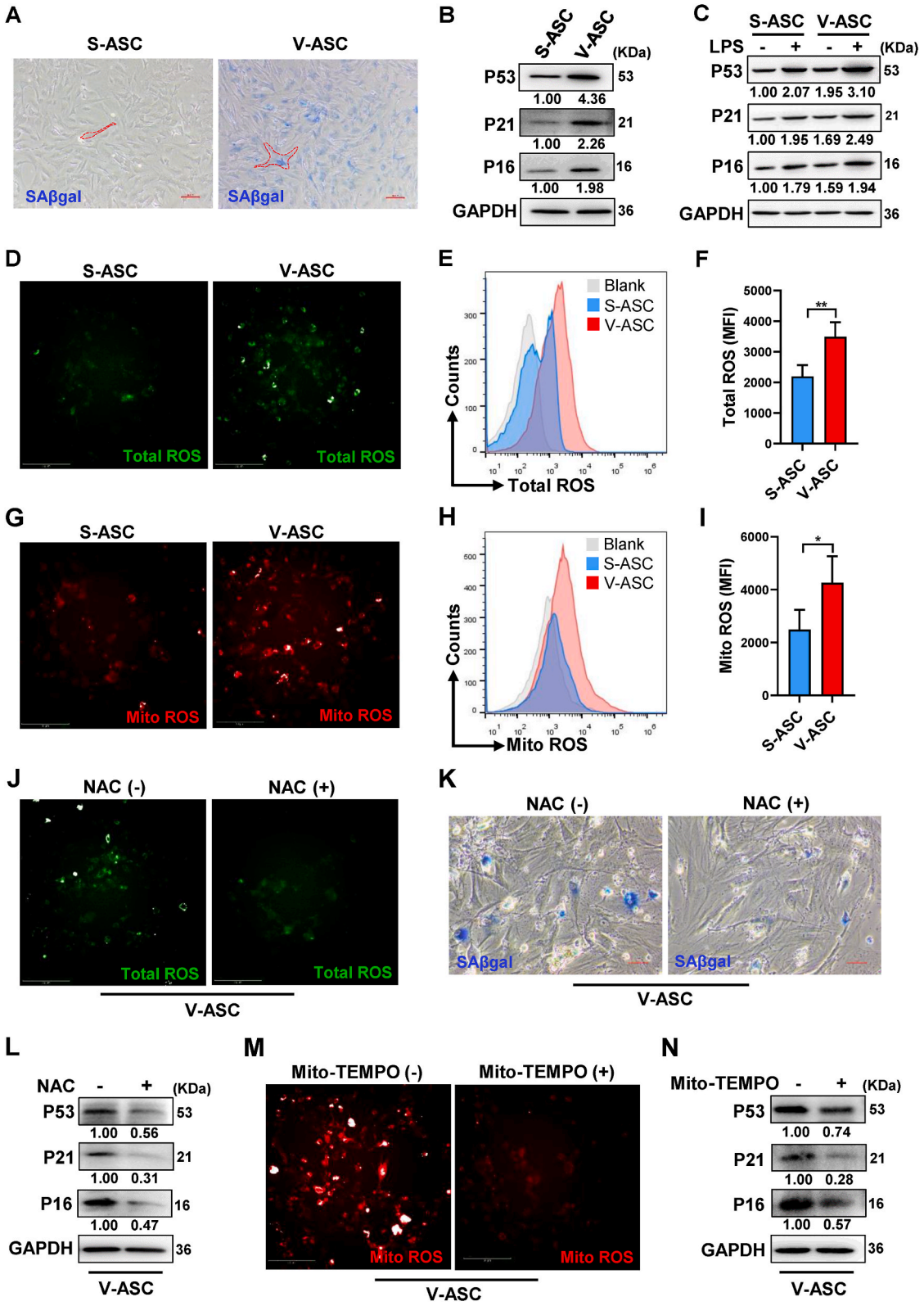

Fig. 1. V-ASCs are prone to senescence caused by intracellular ROS overload

(A and B) Representative SAβgal staining (A) and western blots of P53, P21 and P16 proteins (B) in the third passage of S-ASCs and V-ASCs after 24 h culture. Scale bars, 100 μm. **(C)** Western blots of P53, P21 and P16 proteins in S-ASCs and V-ASCs treated with or without 500 ng/mL LPS for 24 h. **(D–I)** Representative confocal images (D, G), flow cytometry frequency (E, H) and mean fluorescence intensity (MFI) (F, I, n = 4 per group) of total intracellular and mitochondrial ROS in S-ASCs and V-ASCs after 9 h culture. Scale bars, 250 μm. **(J–L)** Representative confocal images for total intracellular ROS (J; Scale bars, 250 μm), SAβgal staining (K; Scale bars, 50 μm) and western blots for indicated proteins (L) in V-ASCs treated with or without 5 mM NAC for 12 h. **(M and N)** Representative confocal images for mitochondrial ROS (M) and western blots for indicated proteins (N) in V-ASCs treated with 5 μM Mito-TEMPO for 12 h. Scale bars, 250 μm. Data are representative of 2 or 3 individual experiments, and presented as mean ± SD. *$p < 0.05$, **$p < 0.01$.

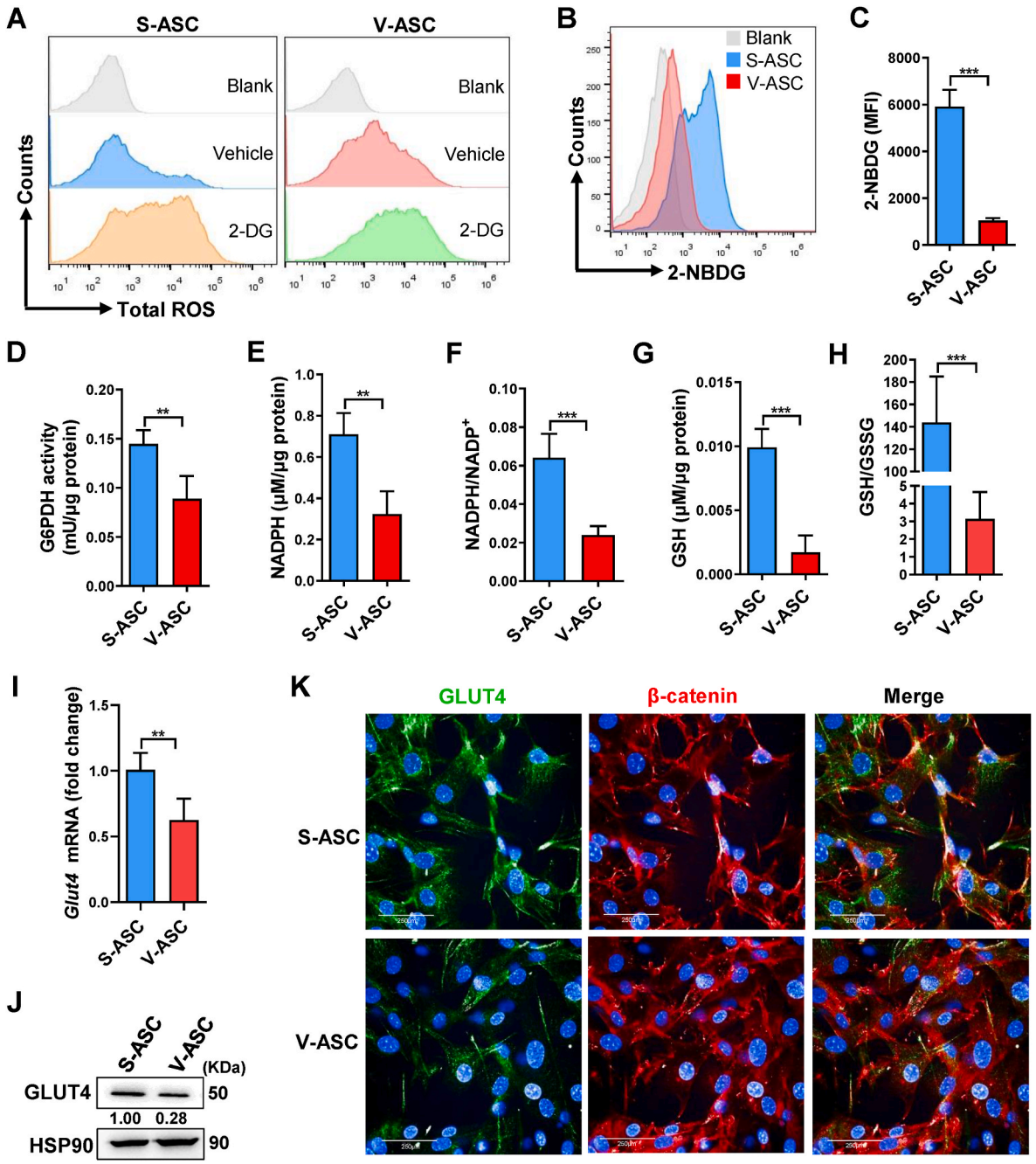

Fig. 2. Inefficient glucose influx disrupts redox homeostasis in V-ASCs by attenuating pentose phosphate pathway
(A) Flow cytometry frequency of total ROS in S-ASCs and V-ASCs treated with 10 mM 2-DG for 8 h. **(B and C)** Flow cytometry frequency (B) and MFI (C, n = 4 per group) of 2-NBDG in S-ASCs and V-ASCs. **(D–H)** G6PDH activity (D), NADPH content (E), NADPH/NADP$^+$ ratio (F), GSH content (G) and GSH/GSSG ratio (H) in S-ASCs and V-ASCs (n = 4 per group). **(I–K)** GLUT4 mRNA (I, n = 6 per group) and protein determined by western blot (J) and confocal imaging (K) in S-ASCs and V-ASCs. GLUT4 (green), β-catenin (red), Nucleus (DAPI, blue) in K. Scale bars, 250 μm. Data are representative of 2 or 3 individual experiments, and presented as mean ± SD. $^{**}p < 0.01$, $^{***}p < 0.001$. (For interpretation of the references to color in this figure legend, the reader is referred to the Web version of this article.)

3. Results

3.1. V-ASCs are prone to senescence caused by intracellular ROS overload

Considering that V-ASCs had relatively poor potentials for *in vitro* proliferation and adipogenic differentiation relative to S-ASCs [7,17], we investigated the senescent characteristics of V-ASCs in comparison with S-ASCs. V-ASCs and S-ASCs at the same passage exhibited significant differences in cell size and morphology. V-ASCs displayed a more senescent morphology, characterized by a larger, flatter and more irregular shape, differing from the small and regular spindle shape of S-ASCs. Importantly, V-ASCs showed more senescent phenotypes than S-ASCs, as suggested by relatively high SAβgal activity and protein levels of P53, P21 and P16 (Fig. 1A and B), indicating that V-ASCs are prone to senescence relative to S-ASCs. In line with this, V-ASCs expressed higher levels of senescence-associated secretory phenotypes (SASPs) than S-ASCs, such as proinflammatory cytokines *Il-1β*, *Il-6* and *Tnf-α* mRNA (Fig. S1A). In particular, V-ASCs secreted a large amount of IL-6 compared with S-ASCs; while either V-ASCs or S-ASCs produced a few of TNF-α, and no significant difference was observed (Fig. S1B). TLRs, the pattern recognition receptors of innate immune cells, have been

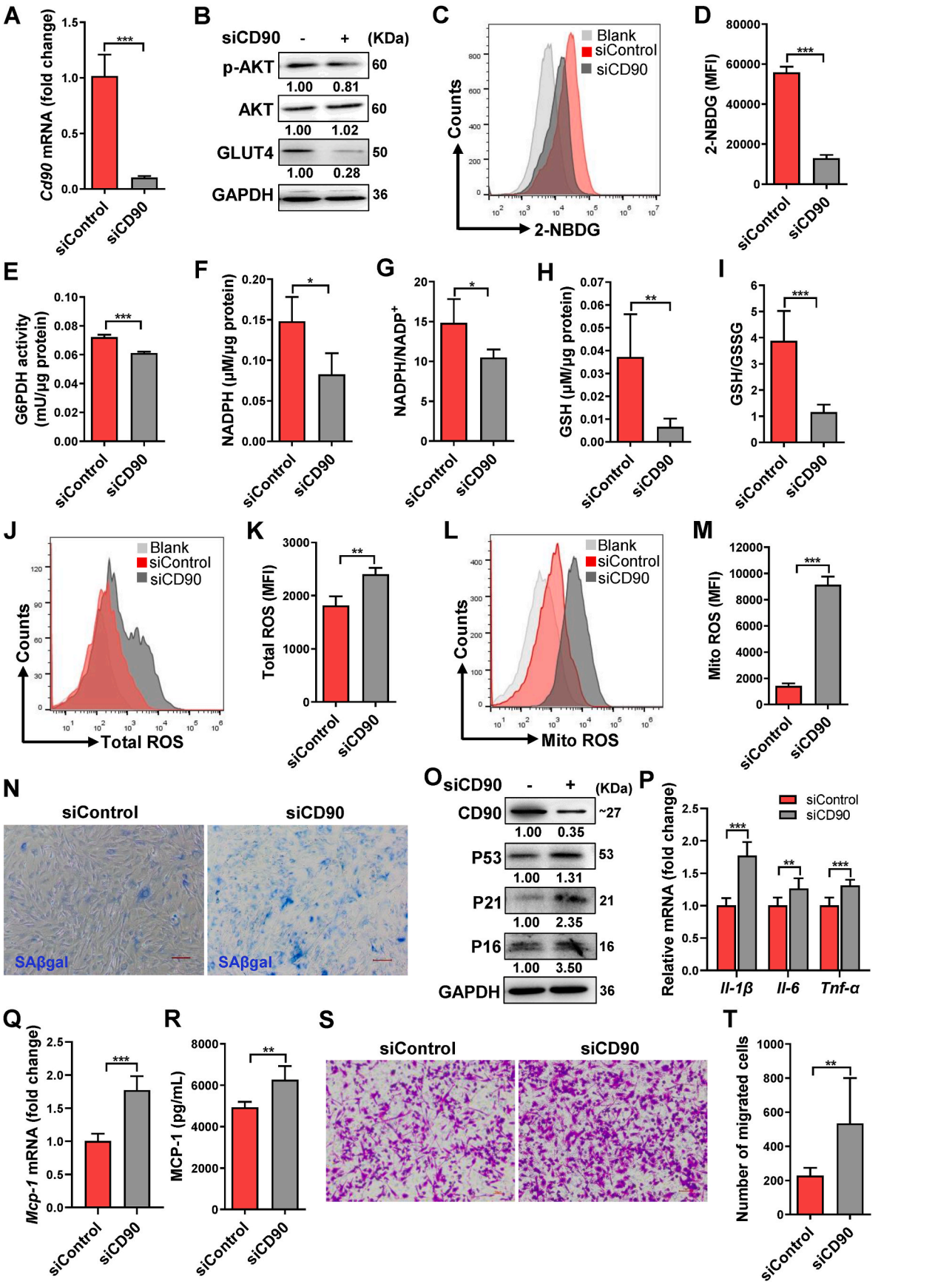

(caption on next page)

Fig. 3. CD90 knockdown induces ASC senescence via restraining glucose influx and PPP-dependent redox homeostasis
(A-D) *Cd90* mRNA (A, n = 5 or 6 per group), representative blots for indicated proteins (B) and glucose uptake determined by flow cytometry (C, D, n = 4 per group) in siCD90-treated V-ASCs. **(E–I)** G6PDH activity (E), NADPH content (F), NADPH/$NADP^+$ ratio (G), GSH content (H) and GSH/GSSG ratio (I) in siCD90-treated V-ASCs (n = 4 or 6 per group). **(J–M)** Flow cytometry frequency and MFI of total (J, K, n = 4 per group) and mitochondrial (L, M, n = 4 per group) ROS in siCD90-treated V-ASCs. **(N–P)** Representative SAβgal staining (N), blots for indicated proteins (O) and mRNA levels of *Il-1β*, *Il-6, Tnf-α* (P, n = 6 per group) in siCD90-treated V-ASCs. Scale bars, 50 μm. **(Q and R)** The mRNA (Q, n = 6 per group) and secretion (R, n = 4 per group) levels of MCP-1 in siCD90-treated V-ASCs. **(S and T)** Representative images (S) and quantification (T, n = 10 per group) for 6 h of macrophage chemotaxis by siCD90-treated ASCs. Scale bars, 20 μm. Data are representative of 2 or 3 individual experiments, and presented as mean ± SD. $^*p < 0.05$, $^{**}p < 0.01$, $^{***}p < 0.001$.

found in adipocytes to mediate inflammatory reaction [34,35]. Intriguingly, V-ASCs expressed higher levels of TLR2 and TLR4 than S-ASCs (Figs. S1C and D). And blockade of TLR2 or TLR4 in V-ASCs using CUCPT-22 or TAK-242 significantly downregulated the mRNA levels of *Il-1β*, *Il-6* and *Tnf-α* (Figs. S1E–G), indicating that TLR2 and TLR4 are critical for SASP expression in resting V-ASCs. Furtherly, treatment with corresponding ligand LPS, induced marked increase of P53, P21 and P16 proteins in V-ASCs compared with S-ASCs (Fig. 1C), indicating that V-ASCs are vulnerable to senescence in response to LPS stimulation. Accordingly, upon LPS challenge, V-ASCs expressed higher levels of *Il-1β*, *Il-6* and *Tnf-α* mRNA, especially secreted significantly higher levels of IL-6 and TNF-α than S-ASCs (Fig. S1H-L). Thus, V-ASCs are more sensitive to senescence and SASP production upon TLR engagement.

To clarify why V-ASCs are prone to senescence, we next examined their intracellular ROS, because oxidative stress is a pivotal inducer of cellular senescence. As suggested by confocal fluorescence imaging and flow cytometry data, V-ASCs had higher levels of total and mitochondrial ROS than S-ASCs (Fig. 1D–I), indicating that V-ASCs are overloaded with intracellular especially mitochondrial ROS. Importantly, removal of intracellular ROS by NAC remarkably decreased the SAβgal activity and the protein levels of P53, P21 and P16 in these senescent V-ASCs (Fig. 1J-L). Likewise, inhibition of mitochondrial ROS by Mito-TEMPO also dramatically reduced P53, P21 and P16 proteins in V-ASCs (Fig. 1M and N). These findings demonstrate that the accumulation of intercellular ROS, especially mitochondrial ROS, is the primary cause for V-ASC senescence.

3.2. Inefficient glucose influx disrupts redox homeostasis in V-ASCs by attenuating pentose phosphate pathway

We then asked why ROS was excessively accumulated in V-ASCs rather than S-ASCs. In several tumor cells, glucose was utilized to maintain redox homeostasis through the pentose phosphate pathway (PPP) [36,37]. To ascertain the possible influence of glucose metabolism on ASC redox status, we utilized glucose analog 2-DG to competitively block glucose influx in ASCs, and found a marked increase of total ROS in either S-ASCs or V-ASCs (Fig. 2A). These data suggest that glucose influx is essential for ASCs to eliminate ROS. We then wondered if V-ASCs had some difficulty to access glucose and thereby caused ROS overload. To test this, we examined the glucose uptake by ASCs using 2-NBDG. Compared with S-ASCs, V-ASCs showed a significant reduction in 2-NBDG uptake (Fig. 2B and C), indicative of inefficient glucose influx in these V-ASCs. Glucose influx can drive effective PPP to maintain cellular redox homeostasis, where G6PDH, the PPP rate-limiting enzyme, determines the NADPH production and subsequent GSH homeostasis to clear excessive ROS. Of note, compared with S-ASCs, V-ASCs showed a significant decrease in G6PDH activity, NADPH content and NADPH/$NADP^+$ ratio; accordingly, the GSH content and GSH/GSSG ratio were reduced in these V-ASCs (Fig. 2D–H). As such, an inefficient glucose influx into PPP may cause GSH imbalance and ROS overload in V-ASCs. We then asked why V-ASCs had difficulty to obtain glucose. Through examining the glucose transporter 4 (GLUT4) in ASCs, we found that V-ASCs had a decrease of GLUT4 on mRNA and protein levels compared with S-ASCs (Fig. 2I and J). Consistently, different from abundant membrane GLUT4 on S-ASCs, few GLUT4 was detectable on V-ASC membranes (Fig. 2K). Thus, the low level of GLUT4 on V-ASCs could restrict the glucose influx into PPP, thereby causing redox imbalance and ROS overload in these cells.

3.3. CD90 knockdown induces ASC senescence via restraining glucose influx and PPP-dependent redox homeostasis

AKT activation is recognized to promote GLUT4 expression and membrane translocation in cells like 3T3-L1 adipocyte and skeletal muscle; and V-ASCs showed an attenuation of AKT activation compared with S-ASCs [17,38–41]. We blocked AKT activation with MK2206 and found a reduction of GLUT4 protein in either V-ASCs or S-ASCs (Fig. S2A), supporting that AKT activation is required for GLUT4 expression in ASCs. We previously demonstrated that stem cell-related marker CD90 could promote AKT activation in ASCs [17]. To test if CD90 could master glucose influx via the AKT-GLUT4 axis in ASCs, we knocked down CD90 in ASCs and found the GLUT4 reduction accompanied by AKT deactivation in either V-ASCs or S-ASCs (Fig. 3A and B, Figs. S2B and C). Importantly, CD90 silence led to significant decrease in 2-NBDG uptake and overall inhibition in G6PDH activity, NADPH content and NADPH/$NADP^+$ ratio in V-ASCs (Fig. 3C–G), suggesting that CD90 is required for effective glucose uptake and PPP in V-ASCs. As a result, GSH content and GSH/GSSG ratio were accordingly reduced by CD90 silence in V-ASCs (Fig. 3H and I), indicative of the crucial role of CD90 in maintaining GSH homeostasis. Similarly, CD90 knockdown also reduced PPP and GSH balance in S-ASCs, as suggested by decreases in G6PDH activity, NADPH/$NADP^+$ ratio, GSH content and GSH/GSSG ratio (Figs. S2D–G). In line with the glucose and GSH dysregulation, CD90 silence in V-ASCs induced marked increase in total and mitochondrial ROS, and elevation in SAβgal activity, protein levels of P53, P21, P16 and mRNA levels of *Il-1β*, *Il-6* and *Tnf-α* (Fig. 3J-P). Besides, CD90 silence in V-ASCs significantly upregulated the mRNA and secretion levels of MCP-1, another SASP, which elicited an increase of macrophage chemotaxis by these ASCs (Fig. 3Q-T). As such, CD90 downregulation may contribute to MCP-1 secretion from ASCs that mediate macrophage recruitment into VAT. Taken together, these findings demonstrate that CD90 may serve as a valve on ASCs that facilitates sufficient glucose influx into PPP and subsequent redox homeostasis, thereby preventing ASC senescence. It is plausible that CD90 downregulation may deprive V-ASCs of glucose and thereby cause ASC senescence.

3.4. FGF21 alleviates V-ASC senescence by promoting CD90 glycosylation to drive glucose influx

Previous studies showed that FGF21 could promote insulin-independent glucose uptake in human primary (or 3T3-L1) adipocytes [23,42]. Given that ASCs relied on their glucose influx to resist senescence, we asked if FGF21 could relieve ASC senescence by improving glucose metabolism. Excitingly, FGF21 treatment dramatically promoted the glucose uptake by V-ASCs, and this glucose influx brought an obvious decrease of intracellular and mitochondrial ROS (Fig. 4A–F). As a consequence, P53, P21, P16 proteins and SAβgal activity were significantly reduced by FGF21 in these V-ASCs (Fig. 4G and H). These observations suggest that FGF21 may promote glucose influx to maintain redox homeostasis and prevent ASC senescence. Previous study showed that FGF21 induced transient ERK activation via FGFR1, and upregulated GLUT1 expression in adipocytes [42–44]. To clarify how FGF21 regulated the glucose influx in ASCs, we further examined its

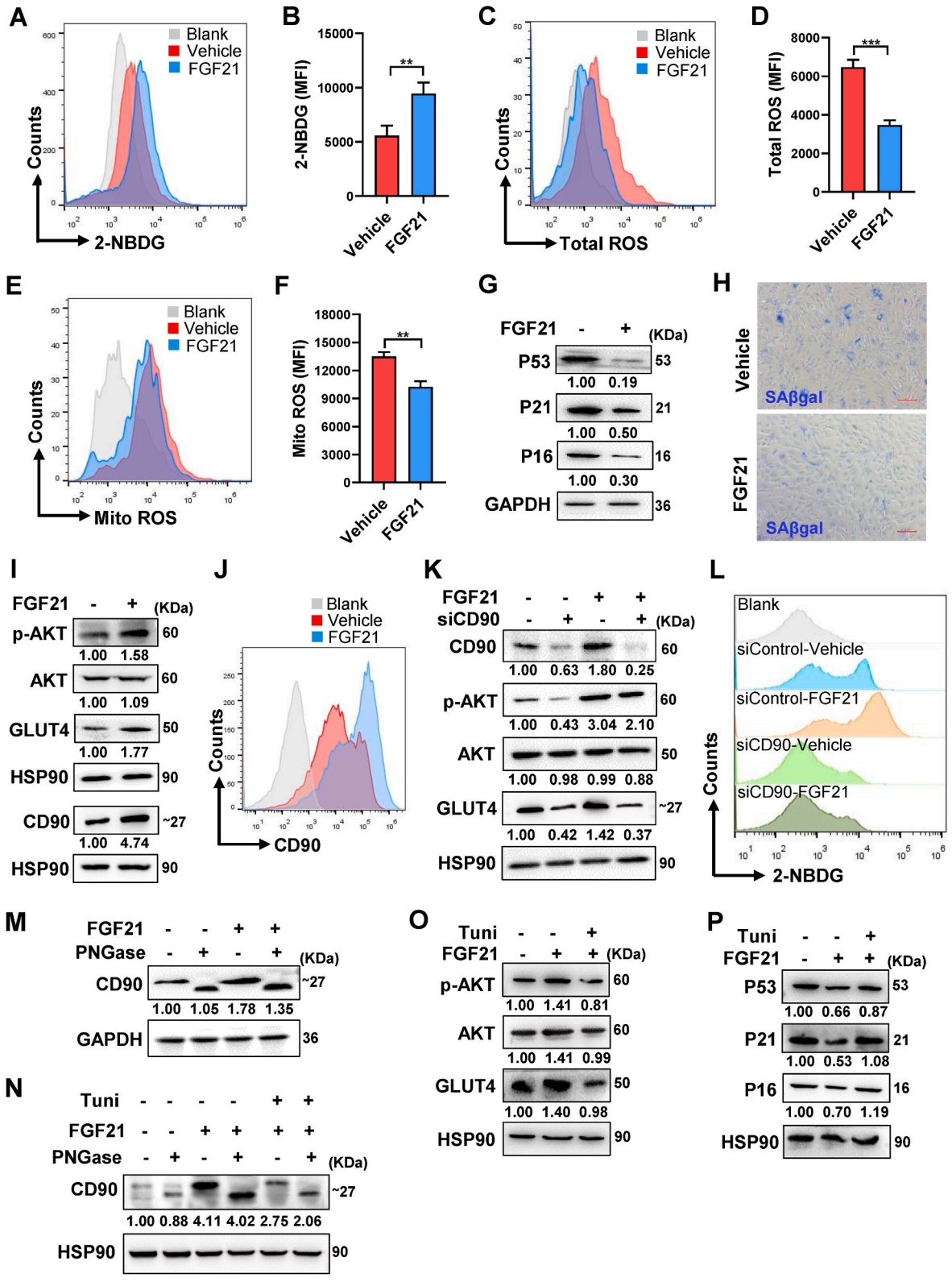

Fig. 4. FGF21 alleviates V-ASC senescence by promoting CD90 glycosylation to drive glucose influx
(A and B) Flow cytometry frequency (A) and MFI (B, n = 4 per group) of 2-NBDG in V-ASCs treated with 500 ng/mL FGF21 for 6 h. **(C–F)** Flow cytometry frequency and MFI of total (C, D, n = 4 per group) and mitochondrial (E, F, n = 4 per group) ROS in V-ASCs treated with 500 ng/mL FGF21 for 12 h. **(G and H)** Representative blots of P53, P21 and P16 proteins (G) and SAβgal staining (H) in V-ASCs treated with FGF21 for 6 h. Scale bars, 30 μm. **(I and J)** Representative blots of *p*-AKT, AKT, GLUT4, CD90 proteins (I) and flow cytometry frequency of CD90 (J) in V-ASCs treated with FGF21 for 6 h. **(K and L)** Representative blots for indicated proteins (K) and flow cytometry frequency of 2-NBDG (L) in siCD90-treated V-ASCs that were stimulated with FGF21 for 6 h. **(M)** Representative blots of CD90 N-glycosylation in FGF21-treated V-ASCs in the presence or absence of PNGase for 2 h at 37 °C. **(N–P)** Representative blots of CD90 N-glycosylation (N) and indicated proteins (O, P) in V-ASCs pretreated with or without 1 μg/mL Tuni for 6 h followed by FGF21 treatment for additional 6 h. Data are representative of 2 or 3 individual experiments, and presented as mean ± SD. $^{**}p < 0.01$, $^{***}p < 0.001$.

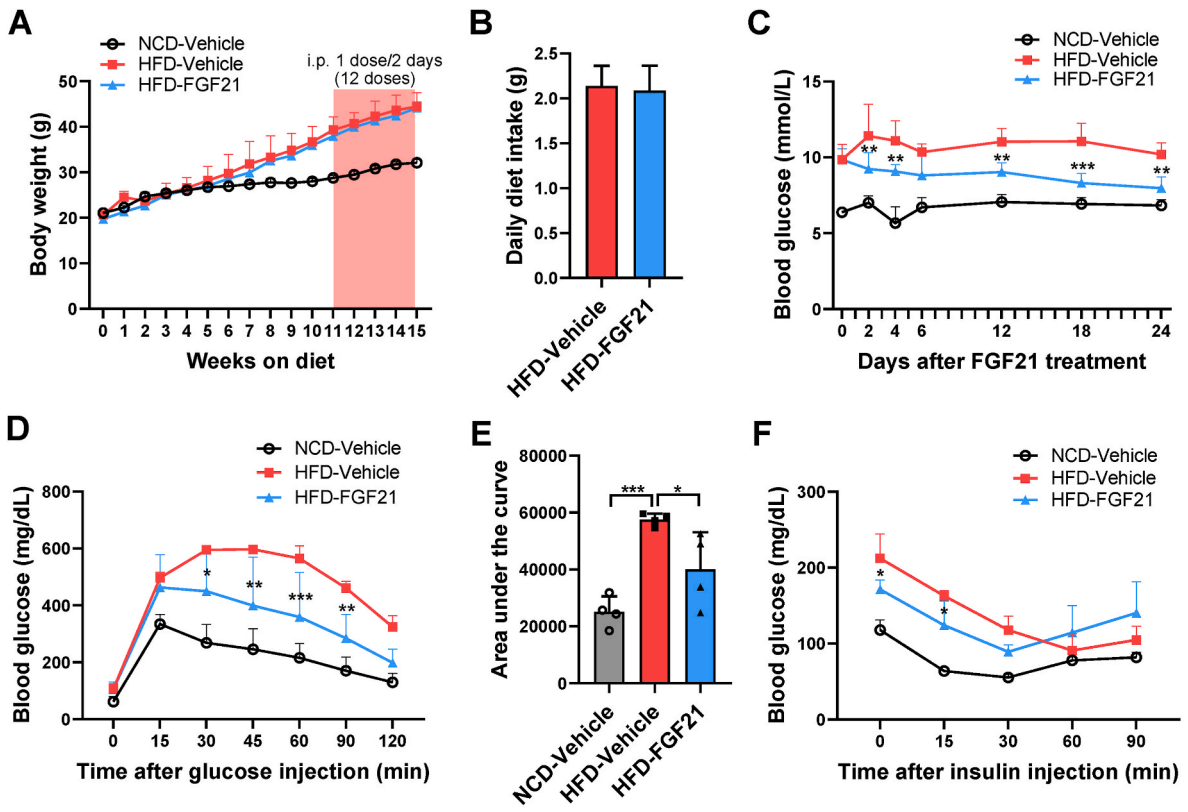

Fig. 5. Chronic FGF21 treatment corrects metabolic disorders in obese mice
(A) Body weight change in mice (n = 4 per group) fed on 15 weeks of NCD or HFD that were intraperitoneally injected with FGF21 (0.5 mg/kg body weight, every 2 days) during the last 4 weeks. **(B and C)** Diet intake (B, n = 6 per group) and blood glucose (C) in mice (n = 4 per group) during FGF21 intervention. **(D–F)** GTT with the area under the curve (D, E) and ITT (F) in mice (n = 4 per group) during the last week of FGF21 intervention. Data are presented as mean ± SD. $*p < 0.05$, $**p < 0.01$, $***p < 0.001$ (HFD-FGF21 vs. HFD-Vehicle in C, D, F).

influences on related glucose transport pathways. Surprisingly, aside from the enhancement of ERK-GLUT1 axis, AKT activation and GLUT4 expression were also increased by FGF21 in these V-ASCs (Fig. 4I, Figs. S3A and B), indicating that FGF21 can augment the AKT-GLUT4 axis of ASCs. Of note, FGF21 treatment caused a robust increase in total and membrane CD90 in these V-ASCs (Fig. 4I and J). But in CD90-silenced V-ASCs, FGF21-elicted AKT activation, GLUT4 elevation and glucose uptake were largely abrogated (Fig. 4K and L), indicating that CD90 is an indispensable target for FGF21 action in V-ASCs. We then asked if ERK activation affected CD90 level and AKT-GLUT4 axis in FGF21-treated V-ASCs. Intriguingly, ERK blockade with U0126 not only inhibited GLUT1 upregulation, but also strongly restrained AKT activation and GLUT4 elevation that were induced by FGF21 in V-ASCs; particularly, FGF21-induced CD90 upregulation was markedly abolished by U0126 treatment (Figs. S3C and D), indicating that FGF21 can augment CD90 protein and AKT-GLUT4 axis via potentiating ERK signaling.

CD90 is a highly glycosylated membrane protein that has two or three N-glycosylated sites in human or mouse, respectively [45]. Effective glucose influx could promote proper expression and membrane localization of specific proteins via N-glycosylation in some cancer cells [46]. Given the activation of ERK-GLUT1 axis by FGF21, we speculated that a rapid glucose influx might promote CD90 N-glycosylation and its protein expression on FGF21-treated V-ASCs. To test this, we treated the protein lysates with PNGase to remove N-glycosylation, and found that the molecular weight of CD90 was apparently reduced in either vehicle- or FGF21-treated V-ASCs (Fig. 4M). This demonstrates that FGF21 plays a critical role in promoting CD90 N-glycosylation. In support of this, the mRNA levels of *Gfat* and *Dpagt1*, two key enzymes responsible for N-glycosylation, were significantly upregulated by FGF21 in V-ASCs (Fig. S3E), implying that FGF21 may promote N-glycosylation process in V-ASCs. More importantly, treatment with N-glycosylation inhibitor tunicamycin (Tuni) remarkably restrained the upregulation of CD90 protein by FGF21 in V-ASCs (Fig. 4N). Accordingly, Tuni treatment counteracted the beneficial effects of FGF21 on augmenting AKT-GULT4 axis and repressing P53, P21, P16 proteins in V-ASCs (Fig. 4O and P), confirming that CD90 N-glycosylation is the key target for FGF21 to alleviate ASC senescence. Altogether, these findings demonstrate that FGF21 may promote CD90 glycosylation expression to potentiate AKT-GLUT4 axis, thereby promoting glucose influx to eliminate ROS overload and alleviate V-ASC senescence.

3.5. *Chronic FGF21 treatment alleviates ASC senescence to remodel healthy VAT and correct metabolic disorders in obese mice*

To test if this desired effect of FGF21 could curb obesity-associated metabolic disorders *in vivo*, we applied chronic administration of low-dose FGF21 into HFD-fed mice. This administration strategy had no obvious influence on weight gain or food intake in mice fed on HFD, but continuously decreased their blood glucose levels during the intervention period (Fig. 5A–C). Importantly, FGF21 treatment significantly reduced the blood glucose levels in HFD-fed mice upon glucose or insulin injection (Fig. 5D–F). In terms of VAT homeostasis, HFD induced an increase of VAT mass, while FGF21 treatment only caused a slight but not significant decrease (Fig. 6A). Of note, HFD feeding in mice severely enhanced the SAβgal activity of VAT, which was obviously diminished by FGF21 treatment (Fig. 6B), suggesting that FGF21 could effectively relieve VAT senescence in mice challenged with HFD. Accordingly, VAT inflammation induced by HFD, including high levels of *Il-1β*, *Il-6,* and *Tnf-α* mRNA, was attenuated by FGF21 treatment in these mice

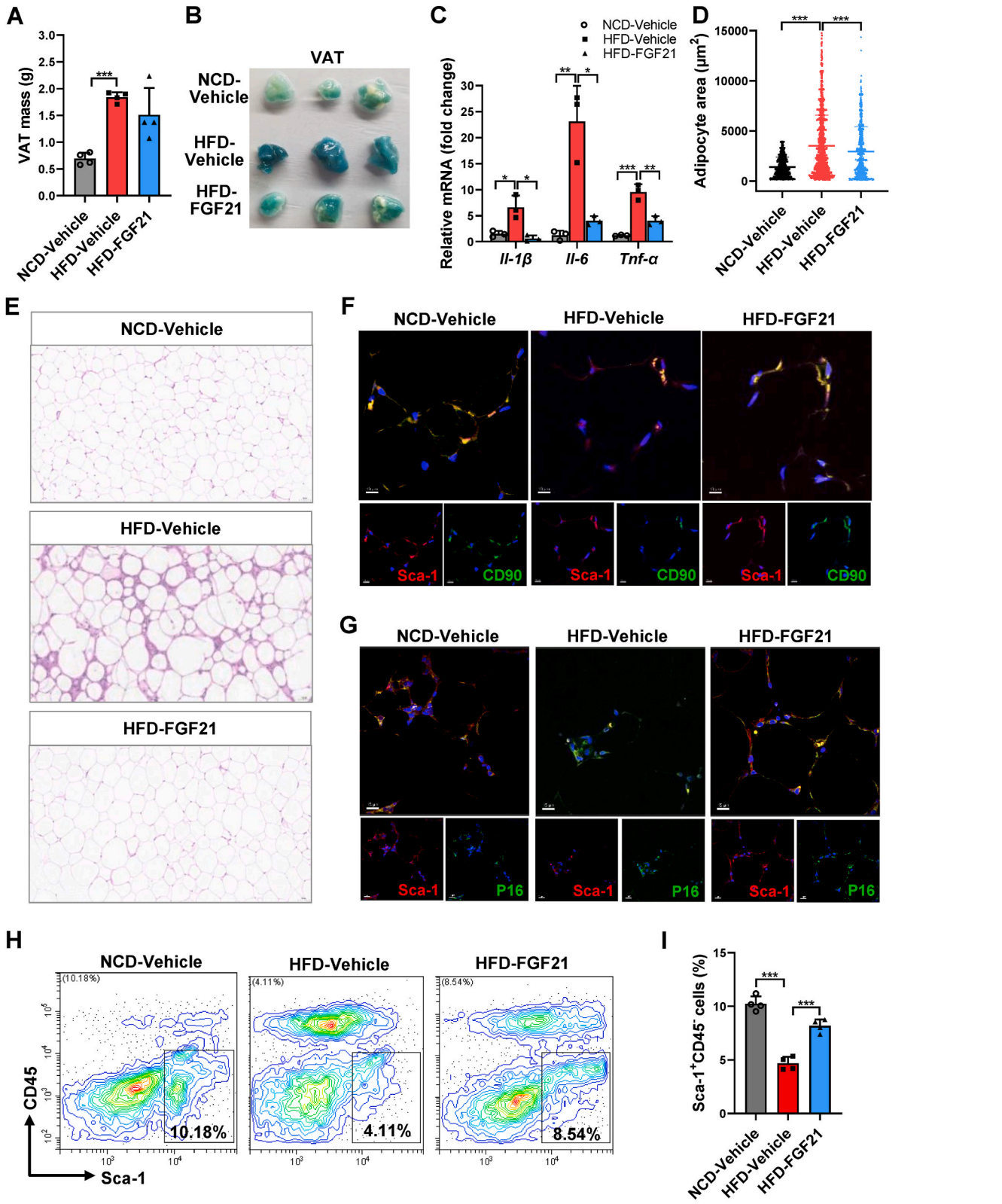

Fig. 6. Chronic FGF21 treatment alleviates ASC senescence to remodel healthy VAT in obese mice
(A) VAT mass in NCD- or HFD-fed mice (n = 4 per group) with or without FGF21 administration. **(B and C)** Staining images for SAβgal activity (B) and mRNA levels of *Il-1β*, *Il-6*, *Tnf-α* (C) in VAT (n = 3 mice per group). **(D and E)** Adipocyte sizes (D, n = at least 400 adipocytes in 2 sections per mouse, 3 mice per group) and representative H&E staining images (E) in VAT sections (n = 3 mice per group). Scale bars, 50 μm. **(F and G)** Representative confocal images for CD90 (green) (F) or P16 (green) (G) proteins in VAT ASCs (Sca-1, red) (n = 3 mice per group). Nucleus (DAPI, blue). Scale bar, 10 μm. **(H and I)** Representative flow cytometry (H) and frequency of Sca-1^{+}CD45^{-} ASCs (I) in SVF from VAT of the mice (n = 4 per group). Data are presented as mean ± SD. $^{*}p < 0.05$, $^{**}p < 0.01$, $^{***}p < 0.001$. (For interpretation of the references to color in this figure legend, the reader is referred to the Web version of this article.)

(Fig. 6C). Furtherly, VAT sections from HFD-fed mice showed obvious adipocyte hypertrophy, which was remarkably mitigated by FGF21 treatment (Fig. 6D and E). In particular, CD90 on the Sca-1$^+$ ASCs of VAT, which was reduced by HFD feeding, was obviously increased by FGF21 treatment; accordingly, P16 on ASCs was elevated by HFD feeding but markedly decreased by FGF21 treatment (Fig. 6F and G). In support of this phenotypic switch of ASCs, the percentage of Sca-1$^+$CD45$^-$ASCs in VAT that was decreased by HFD feeding, was significantly reversed by FGF21 treatment in a large part (Fig. 6H and I). And FGF21 treatment induced an increase of *Pdgfrα* and *Pdgfrβ* mRNA in VAT of HFD-fed mice, while no obvious upregulation of *Prdm16* and *Ucp1* mRNA (Figs. S4A–D), indicating that FGF21 may promote classical adipogenesis in VAT. Altogether, chronic administration of low-dose FGF21 could effectively relieve ASC senescence and remodel VAT homeostasis, thereby correcting metabolic disorders in HFD-fed mice.

4. Discussion

ASCs serve as the pivotal reservoir for adaptive adipocyte hyperplasia in heathy WAT remodeling [2,21]. It is plausible that senescent ASCs are difficult to drive adipogenesis and thereby interrupt WAT homeostasis and metabolic balance. We showed that V-ASCs were prone to senescence and SASP production, mainly caused by oxidative stress from ROS overload. These observations were largely in agreement with the high risk of unhealthy VAT remodeling upon obesity challenge. Using ROS overloaded or depleted 3T3-L1 adipocytes or mouse models, several studies demonstrated that oxidative stress could impair adipogenesis or disrupt healthy adipose expansion and WAT remodeling [47,48]. In support of the above findings, our study adds ASC senescence on the intersection of oxidative stress and pathological VAT remodeling. We reveal that ASCs rely on effective glucose influx into PPP to reduce ROS overload and resist senescence. This metabolic requirement for glucose availability was very similar to that of some tumor cells, which facilitated redox homeostasis to avoid senescence or death [36,37]. As such, the potential strategy to combat ASC senescence is to drive effective glucose influx to maintain redox homeostasis. CD90 is constitutively expressed on mesenchymal stem cells (MSCs) from different murine and human tissues, and thus is widely used as one of MSC markers for identification [49,50]. Our previous study showed that mouse V-ASCs had a lower level of CD90 than S-ASCs, and CD90 protein was decreased in VAT of obese mice [5,17]. Regardless of its impact on other MSCs from different sources, CD90 expression endows human or mouse ASCs with high capacities for proliferation and adipogenic differentiation and thereby determines their adipogenesis [17,51,52]. Besides this, it is largely unclear whether CD90 could influence glucose metabolism or ASC senescence. Here, we showed that CD90 silence elicited senescent phenotypes in ASCs, accompanied by alterations in glucose metabolism and redox status, including reduced glucose uptake, decreased NADPH, GSH levels and increased ROS accumulation. These data provide evidence that abundant CD90 is indispensable to drive glucose metabolism into PPP and thereby maintain redox homeostasis. So, CD90 may be a promising intervention target to counteract ASC senescence.

Previous studies showed that FGF21 could promote insulin-independent glucose uptake by 3T3-L1 adipocytes or human primary adipocytes, but its roles in primary ASCs remain uncertain [23,53]. We treated V-ASCs with FGF21 and unexpectedly found a robust increase of glucose uptake but a decrease of intracellular ROS. As expected, the senescent phenotypes were simultaneously abolished in these ASCs. Interestingly, FGF21 treatment not only enhanced the ERK-GLUT1 axis, which was a transient effect mediated by FGF21 receptors [23], but also augmented the AKT-GLUT4 axis in ASCs. More surprisingly, FGF21 remarkably upregulated CD90, probably a contributor to AKT-GLUT4 enhancement in ASCs, as CD90 could promote AKT activation through recruiting its PH (pleckstrin homology) domain to cell membrane [17]. Indeed, CD90 silence abrogated the augmentation of AKT-GLUT4 axis and glucose uptake in ASCs induced by FGF21, confirming that FGF21 can boost glucose influx via the CD90-AKT-GLUT4 pathway. This process was independent of insulin and different from the insulin-driven glucose uptake via mTORC1 activation in FGF21-treated 3T3-L1 adipocytes [54]. More importantly, FGF21 upregulated CD90 protein on ASCs by promoting its N-glycosylation, while blockade of CD90 N-glycosylation offset the AKT-GLUT4 enhancement and the senescence resistance induced by FGF21 in these ASCs. N-glycosylation modification on specific proteins via the addition of N-acetylglucosamine (GlcNAc) is an important pathophysiological process that ensures proper protein structure and subcellular location, which requires the addition or removal of various glucose or other monosaccharides during GlcNAc formation [55,56]. It has been reported that effective glucose influx in some cancer cells could promote N-glycosylation of specific protein to allow its proper membrane localization [46]. In our study, it is plausible that FGF21 may initiate a rapid glucose influx via the ERK-GLUT1 axis, which increases CD90 glycosylation expression and then activates the AKT-GLUT4 axis to boost glucose influx, thereby promoting glucose metabolism into PPP and ensuing redox homeostasis to inhibit ASC senescence.

Previous studies showed that *in vivo* FGF21 administration in obese mouse models elicited beneficial metabolic improvement whilst brought some undesired effects. Acute FGF21 administration on mg levels per kg body weight induced significant glucose-lowering effect in *ob/ob* mice, but this effect was only maintained 3–24 h. And chronic administration of high-dose FGF21 (up to 10 mg/kg body weight, twice daily) mediated weight loss and insulin sensitivity in diet-induced obese mice. It is believed that this FGF21-induced weight loss is caused by its action on central nervous system, such as affecting food intake or activating sympathetic nervous system [19,25,26,57]. In our obese mouse models, we administrated low-dose FGF21 (0.5 mg/kg body weight) every other day. This mild intervention strategy successfully improved metabolic homeostasis of the mice, and importantly, did not affect their body weight and food intake. More importantly, this FGF21 intervention effectively alleviated VAT senescence and promoted healthy VAT remodeling in obese mice. These metabolic benefits brought by FGF21 could be attributed to its anti-senescence action on ASCs, as demonstrated by CD90 upregulation but P16 downregulation on VAT ASCs and a restoration of ASC reservoir in these FGF21-treated mice. Therefore, this FGF21 intervention may be a promising strategy to correct ASC senescence in VAT and relieve obesity-associated metabolic dysfunction.

Taken together, our findings reveal an anti-senescence mechanism of ASCs that is driven by efficient glucose influx and ROS removal, and identify CD90 as a pivotal valve to master this process. We propose a FGF21-based strategy that targets CD90 glycosylation to drive efficient PPP, thereby maintaining redox homeostasis to reduce ASC senescence, further promoting healthy VAT remodeling to combat obesity-associated metabolic disorders.

Author contributions

ZZ and H. Zhang designed and performed the study, prepared the manuscript. YT, JZ, JZ, HL, YW and TW performed mouse model experiment and Western blot. H. Zhao, FW, CG and FZ provided resources and technical supports. HM, FL and LZ contribute to data analysis and interpretation. QW conceptualized and supervised the study, wrote the manuscript. All authors approved the final manuscript.

Declaration of competing interest

The authors declare no competing financial interests in this study.

Data availability

Data will be made available on request.

Acknowledgment

This work was supported by National Natural Science Foundation of China grants (81970733, 81770838). And we thank for the Microscopy imaging were performed with Microscopy Characterization Facility (Shandong University, China).

Appendix A. Supplementary data

Supplementary data to this article can be found online at https://doi.org/10.1016/j.redox.2023.102877.

References

[1] M. Shao, et al., De novo adipocyte differentiation from Pdgfrbeta(+) preadipocytes protects against pathologic visceral adipose expansion in obesity, Nat. Commun. 9 (1) (2018) 890.
[2] L. Vishvanath, et al., Contribution of adipogenesis to healthy adipose tissue expansion in obesity, J. Clin. Invest. 129 (10) (2019) 4022–4031.
[3] M. Shao, et al., Pathologic HIF1alpha signaling drives adipose progenitor dysfunction in obesity, Cell Stem Cell 28 (4) (2021) 685–701 e7.
[4] H. Zhao, et al., Exosomes from adipose-derived stem cells attenuate adipose inflammation and obesity through polarizing M2 macrophages and beiging in white adipose tissue, Diabetes 67 (2) (2018) 235–247.
[5] Q. Shang, et al., Delivery of adipose-derived stem cells attenuates adipose tissue inflammation and insulin resistance in obese mice through remodeling macrophage phenotypes, Stem Cell. Dev. 24 (17) (2015) 2052–2064.
[6] A. Chait, et al., Adipose tissue distribution, inflammation and its metabolic consequences, including diabetes and cardiovascular disease, Front. Cardiovasc. Med. 7 (2020).
[7] Y. Macotela, et al., Intrinsic differences in adipocyte precursor cells from different white fat depots, Diabetes 61 (7) (2012) 1691–1699.
[8] Q.A. Wang, et al., Tracking adipogenesis during white adipose tissue development, expansion and regeneration, Nat. Med. 19 (10) (2013) 1338–1344.
[9] N. Mathur, et al., Human visceral and subcutaneous adipose stem and progenitor cells retain depot-specific adipogenic properties during obesity, Front. Cell Dev. Biol. 10 (2022), 983899.
[10] L.M. Perez, et al., Altered metabolic and stemness capacity of adipose tissue-derived stem cells from obese mouse and human, PLoS One 10 (4) (2015), e0123397.
[11] A.K. Palmer, et al., Targeting senescent cells alleviates obesity-induced metabolic dysfunction, Aging Cell 18 (3) (2019), e12950.
[12] K. Shirakawa, et al., Obesity accelerates T cell senescence in murine visceral adipose tissue, J. Clin. Invest. 126 (12) (2016) 4626–4639.
[13] S.M. Conley, et al., Human obesity induces dysfunction and early senescence in adipose tissue-derived mesenchymal stromal/stem cells, Front. Cell Dev. Biol. 8 (2020) 197.
[14] B. Gustafson, et al., Reduced subcutaneous adipogenesis in human hypertrophic obesity is linked to senescent precursor cells, Nat. Commun. 10 (1) (2019) 2757.
[15] D. Munoz-Espin, et al., Cellular senescence: from physiology to pathology, Nat. Rev. Mol. Cell Biol. 15 (7) (2014) 482–496.
[16] B.G. Childs, et al., Cellular senescence in aging and age-related disease: from mechanisms to therapy, Nat. Med. 21 (12) (2015) 1424–1435.
[17] Z. Pan, et al., CD90 serves as differential modulator of subcutaneous and visceral adipose-derived stem cells by regulating AKT activation that influences adipose tissue and metabolic homeostasis, Stem Cell Res. Ther. 10 (1) (2019) 355.
[18] Z. Zhou, et al., CX3CR1(hi) macrophages sustain metabolic adaptation by relieving adipose-derived stem cell senescence in visceral adipose tissue, Cell Rep. 42 (5) (2023), 112424.
[19] K.H. Flippo, et al., Metabolic messengers: FGF21, Nat. Metab. 3 (3) (2021) 309–317.
[20] K.R. Markan, et al., Circulating FGF21 is liver derived and enhances glucose uptake during refeeding and overfeeding, Diabetes 63 (12) (2014) 4057–4063.
[21] F. Louwen, et al., Insight into the development of obesity: functional alterations of adipose-derived mesenchymal stem cells, Obes. Rev. 19 (7) (2018) 888–904.
[22] L. Geng, et al., The therapeutic potential of FGF21 in metabolic diseases: from bench to clinic, Nat. Rev. Endocrinol. 16 (11) (2020) 654–667.
[23] A. Kharitonenkov, et al., FGF-21 as a novel metabolic regulator, J. Clin. Invest. 115 (6) (2005) 1627–1635.
[24] L. Dollet, et al., FGF21 improves the adipocyte dysfunction related to seipin deficiency, Diabetes 65 (11) (2016) 3410–3417.
[25] J. Xu, et al., Fibroblast growth factor 21 reverses hepatic steatosis, increases energy expenditure, and improves insulin sensitivity in diet-induced obese mice, Diabetes 58 (1) (2009) 250–259.
[26] J. Xu, et al., Acute glucose-lowering and insulin-sensitizing action of FGF21 in insulin-resistant mouse models–association with liver and adipose tissue effects, Am. J. Physiol. Endocrinol. Metabol. 297 (5) (2009) E1105–E1114.
[27] L.D. BonDurant, et al., FGF21 regulates metabolism through adipose-dependent and -independent mechanisms, Cell Metabol. 25 (4) (2017) 935–944 e4.
[28] Y. Chen, et al., Adipocyte IRE1α promotes PGC1α mRNA decay and restrains adaptive thermogenesis, Nat. Metab. 4 (9) (2022) 1166–1184.
[29] L.-R. Kong, et al., Loss of C3a and C5a receptors promotes adipocyte browning and attenuates diet-induced obesity via activating inosine/A2aR pathway, Cell Rep. 42 (2) (2023).
[30] N.L. Price, et al., Genetic ablation of miR-33 increases food intake, enhances adipose tissue expansion, and promotes obesity and insulin resistance, Cell Rep. 22 (8) (2018) 2133–2145.
[31] Q. Zhu, et al., Adipocyte mesenchymal transition contributes to mammary tumor progression, Cell Rep. 40 (11) (2022).
[32] T.C.L. Bargut, et al., Fish oil diet modulates epididymal and inguinal adipocyte metabolism in mice, Food Funct. 7 (3) (2016) 1468–1476.
[33] H. Kurosu, et al., Tissue-specific expression of betaKlotho and fibroblast growth factor (FGF) receptor isoforms determines metabolic activity of FGF19 and FGF21, J. Biol. Chem. 282 (37) (2007) 26687–26695.
[34] A. Batra, et al., Leptin-dependent toll-like receptor expression and responsiveness in preadipocytes and adipocytes, Am. J. Pathol. 170 (6) (2007) 1931–1941.
[35] A. Kopp, et al., Innate immunity and adipocyte function: ligand-specific activation of multiple Toll-like receptors modulates cytokine, adipokine, and chemokine secretion in adipocytes, Obesity 17 (4) (2009) 648–656.
[36] N.A. Graham, et al., Glucose deprivation activates a metabolic and signaling amplification loop leading to cell death, Mol. Syst. Biol. 8 (2012) 589.
[37] E. Favaro, et al., Glucose utilization via glycogen phosphorylase sustains proliferation and prevents premature senescence in cancer cells, Cell Metabol. 16 (6) (2012) 751–764.
[38] A. Chadt, et al., Glucose transporters in adipose tissue, liver, and skeletal muscle in metabolic health and disease, Pflügers Archiv 472 (9) (2020) 1273–1298.
[39] P. Manna, et al., PIP3 but not PIP2 increases GLUT4 surface expression and glucose metabolism mediated by AKT/PKCzeta/lambda phosphorylation in 3T3L1 adipocytes, Mol. Cell. Biochem. 381 (1–2) (2013) 291–299.
[40] H. Sano, et al., Rab10, a target of the AS160 Rab GAP, is required for insulin-stimulated translocation of GLUT4 to the adipocyte plasma membrane, Cell Metabol. 5 (4) (2007) 293–303.
[41] Y. Wang, et al., Effects of four weeks intermittent hypoxia intervention on glucose homeostasis, insulin sensitivity, GLUT4 translocation, insulin receptor phosphorylation, and Akt activity in skeletal muscle of obese mice with type 2 diabetes, PLoS One 13 (9) (2018), e0203551.
[42] X. Ge, et al., Fibroblast growth factor 21 induces glucose transporter-1 expression through activation of the serum response factor/Ets-like protein-1 in adipocytes, J. Biol. Chem. 286 (40) (2011) 34533–34541.
[43] G. Singhal, et al., Fibroblast growth factor 21 (FGF21) protects against high fat diet induced inflammation and islet hyperplasia in pancreas, PLoS One 11 (2) (2016), e0148252.
[44] W. Wente, et al., Fibroblast growth factor-21 improves pancreatic beta-cell function and survival by activation of extracellular signal-regulated kinase 1/2 and Akt signaling pathways, Diabetes 55 (9) (2006) 2470–2478.
[45] C. Sauzay, et al., CD90/Thy-1, a cancer-associated cell surface signaling molecule, Front. Cell Dev. Biol. 7 (2019) 66.
[46] C. Cheng, et al., Glucose-mediated N-glycosylation of SCAP is essential for SREBP-1 activation and tumor growth, Cancer Cell 28 (5) (2015) 569–581.
[47] Y. Okuno, et al., Oxidative stress inhibits healthy adipose expansion through suppression of SREBF1-mediated lipogenic pathway, Diabetes 67 (6) (2018) 1113–1127.
[48] R. Fernando, et al., Low steady-state oxidative stress inhibits adipogenesis by altering mitochondrial dynamics and decreasing cellular respiration, Redox Biol. 32 (2020), 101507.
[49] A. Saalbach, et al., Thy-1: more than a marker for mesenchymal stromal cells, Faseb. J. 33 (6) (2019) 6689–6696.
[50] E. Jones, et al., Where is the common ground between bone marrow mesenchymal stem/stromal cells from different donors and species? Stem Cell Res. Ther. 6 (1) (2015) 143.
[51] G.A. Ferraro, et al., Human adipose CD34+ CD90+ stem cells and collagen scaffold constructs grafted in vivo fabricate loose connective and adipose tissues, J. Cell. Biochem. 114 (5) (2013) 1039–1049.
[52] H. Martini, et al., Aging induces cardiac mesenchymal stromal cell senescence and promotes endothelial cell fate of the CD90 + subset, Aging Cell 18 (5) (2019), e13015.
[53] S. Justesen, et al., The autocrine role of FGF21 in cultured adipocytes, Biochem. J. 477 (13) (2020) 2477–2487.
[54] A.Y. Minard, et al., mTORC1 is a major regulatory node in the FGF21 signaling network in adipocytes, Cell Rep. 17 (1) (2016) 29–36.
[55] C. Reily, et al., Glycosylation in health and disease, Nat. Rev. Nephrol. 15 (6) (2019) 346–366.
[56] A. Varki, Biological roles of glycans, Glycobiology 27 (1) (2017) 3–49.
[57] T. Coskun, et al., Fibroblast growth factor 21 corrects obesity in mice, Endocrinology 149 (12) (2008) 6018–6027.